https://doi.org/10.1016/j.solener.2019.03.048

Thermal performance improvement using unilateral spiral ribbed absorber tube for parabolic trough solar collector

Bin Zou[a, b], Yiqiang Jiang[a, *], Yang Yao[a], Hongxing Yang[b]

[a] School of Architecture, Harbin Institute of Technology; Key Laboratory of Cold Region Urban and Rural Human Settlement Environment Science and Technology, Ministry of Industry and Information Technology, Harbin, China

[b] Renewable Energy Research Group (RERG), Department of Building Services Engineering, The Hong Kong Polytechnic University, Hong Kong, China

Abstract

Enhancing the heat transfer in the absorber tube improves effectively both the thermal efficiency and the structural safety of the parabolic trough receiver (PTR). This study proposed a novel unilateral spiral ribbed PTR (USR-PTR) for enhancing the heat transfer inside the absorber. The flow and heat transfer performance of the proposed USR-PTR was studied numerically using CFD tool coupled with Monte Carlo Ray Tracing (MCRT). A detailed comparison between the USR-PTR and the conventional straight and smooth PTR (CSS-PTR) was conducted in terms of both thermal and hydraulic performance, revealing that fluid disturbance, rotational flow and local

longitudinal vortexes induced by the discontinuous spiral ribs are the three main causes of heat transfer enhancement in the USR-PTR. In most cases of the discussed flow rates, the overall performance of the USR-PTR is better than that of the CSS-PTR. The circumferential temperature difference of the USR-PTR can be reduced by up to 25% compared to the CSS-PTR. The structural parameters of the spiral rib influence greatly the performance of the USR-PTR. It is revealed that the improvement of the overall performance of the USR-PTR by changing individually the rib structural parameters, including pitch interval, rib height, corner radius and spiral angle, can be up to 12.5%, 9.8%, 10.8% and 30.1% respectively.

Keywords: Parabolic trough solar collector; Thermal performance improvement; Unilateral spiral ribbed absorber tube; Receiver tube; Performance evaluation

* Corresponding authors: School of Architecture, Harbin Institute of Technology; Key Laboratory of Cold Region Urban and Rural Human Settlement Environment Science and Technology, Ministry of Industry and Information Technology, Harbin, China.

E-mail: jyq7245@163.com (Y. Jiang)

Nomenclature

A	area (m^2)
c_1, c_2, c_μ	constants in turbulence model
c_p	specific heat at constant pressure
d	diameter (m)
e	relative error (%)
f	friction factor for USR-PTR
f_0	friction factor for CSS-PTR
f_c	focal length (m)
f_P	friction factor calculated by empirical formula
F_i	mass force components (m/s^2)
h	heat transfer coefficient ($W/m^2 \cdot K$)
Δh	height of the rib (mm)
k	pulsation kinetic energy
L_a	length of the discussed absorber (m)
L_c	length of the LS-2 PTC module (m)
$\dot{m}$	mass flow rate (kg/s)
Nu	Nusselt number for USR-PTR
Nu_0	Nusselt number for CSS-PTR
Nu_G	Nusselt number calculated by empirical formula
p	pitch interval of the rib (mm)
Pr	Prandtl number
ΔP	pressure drop in the absorber (Pa)
q_u	useful energy obtained by the HTF (W)
R_{co}	corner radius of the rib (mm)
R_{cr}	crest radius of the rib (mm)
Re	Reynolds number

T	temperature (K)
u_i	velocity components, (m/s)
v	fluid average velocity (m/s)
W_c	aperture width of the PTC module (m)

Greek symbols

α_a	absorptivity of the selective coating
α_s	spiral angle of the rib (°)
δ_{ij}	Kronecker delta
ε	turbulent dissipation rate
ε_{coa}	emittance of the selective coating
η	time average strain rate (%)
λ	thermal conductivity (W/m·K)
μ	dynamic viscosity (Pa·s)
μ_t	turbulence viscosity (Pa·s)
ρ	density (kg/m^3)
ρ_r	reflectivity of the reflector
σ_ε	Prandtl number for turbulent dissipation rate
σ_k	Prandtl number for turbulent kinetic energy
σ_t	turbulence Prandtl number
τ_g	transmissivity of the glass envelope
φ_a	circle angle of the absorber (°)

Subscripts

a	absorber
amb	ambient
f	fluid
g	glass envelope
i	inner surface

in	inlet
max	maximum
min	minimum
o	outer surface
out	outlet
s	simulation
t	test
x, *y*, *z*	Cartesian coordinates

Abbreviations

CSP	concentrating solar power
CSS-PTR	conventional straight and smooth parabolic trough receiver
FVM	Finite Volume Method
HFC	heliostat field concentrator
HTF	heat transfer fluid
MCRT	Monte Carlo Ray Tracing
PEC	performance evaluation criterion
PDC	parabolic dish collector
PTC	parabolic trough collector
RTM	Ray Tracing Method
UDF	User Defined Functions
USR-PTR	unilateral spiral ribbed parabolic trough receiver

1. Introduction

As the most widely distributed and typical renewable energy, solar energy has been utilized worldwide to meet the growing energy demand and to mitigate the deteriorating ecological environment (Devabhaktuni et al., 2013; Kalogirou, 2003; Wang et al., 2015).

Concentrated solar power (CSP) technology, including parabolic trough collector (PTC), parabolic dish collector (PDC), linear Fresnel collector and heliostat field concentrator (HFC), is one of the promising and developed technologies in utilization of solar energy, having attracted extensive attention (Mills, 2004; Xu et al., 2016). Among the four main CSP technologies, the parabolic trough collector (PTC) technology is the most cost-effective one (Jebasingh et al., 2016; Wang et al., 2017). Apart from power generation, PTCs have also been applied in many other fields, such as industrial process heat production, desalination, refrigeration and air-conditioning (Bermejo et al., 2010; Cabrera et al., 2013; Fernandez-Garcia, et al., 2010; Kalogirou, 1998, 2002; Scrivani et al., 2007), showing great development prospects.

A PTC consists mainly of a parabolic reflector and a receiver tube which is composed of a glass envelope and a metal absorber tube. The annulus between the glass envelope and the absorber tube contains vacuum to reduce heat loss and avoid oxidation of the coating. Due to the sunlight-concentration of the reflector, the reflected rays are mainly focused on the arc of the absorber tube's circumference facing the reflector, leading to extremely uneven heat flux distribution, which results in a large temperature difference around the absorber. The circumferential temperature difference leads to thermal strain, causing thermal deformation of the absorber, which is the main cause of the receiver tube breaking (Almanza et al., 1997; Khanna et al., 2014). Moreover, the peak temperature on parts of the absorber surface may cause local overheating, threatening the stability and reducing the service life of the thermal oil and the coating

(Benoit et al., 2016; Zhang et al., 2017). Thus, the thermal performance of the receiver tube is of great significance to the PTC's safety and stability.

Enhancing the heat transfer in the parabolic trough receiver (PTR) can not only improve the thermal efficiency but also reduce the circumferential temperature difference effectively (Conrado et al., 2017; Sandeep et al., 2017). Numerous heat transfer enhancement methods for the PTR have be proposed and investigated in previous studies. Kumar et al. (2009) and Reddy et al. (2015) conducted both numerical and experimental studies on the thermal performance of the PTR with insertion of porous disc, and drew the conclusion that both the circumferential temperature difference and the heat loss were reduced, while the pressure loss was increased. Munoz et al. (2011) conducted a detailed simulation on the internal finned tubes used in parabolic trough collectors using CFD tool. Their results showed that the circumferential temperature difference decreased by 40% and the thermal loss was reduced by 18%, compared with the conventional straight and smooth PTR (CSS-PTR). Wang et al. (2013) investigated heat transfer enhancement by inserting metal foams in the absorber tube, and presented that the maximum circumferential temperature difference decreased about by 45%. Mwesigye et al. (2014) proposed a new type of PTR with centrally inserted perforated plate and stated that the temperature gradient could be reduced by up to 33%. Ghadirijafarbeigloo et al. (2014) carried out a 3D numerical simulation to study the heat transfer enhancement and turbulent flow of a PTR with louvered twisted-tapes. It was revealed that, compared with the CSS-PTR,

the Nusselt number was 150% higher and the increase of the friction factor has reached the 210% mark. Kalidasan et al. (2016) studied experimentally the performance of the PTR tube with internal hinged blades. It was presented in their work that almost 14% improvement of the average efficiency could be achieved. Wang et al. (2016a, 2016b) introduced the symmetric and asymmetric outward convex corrugated tubes as the absorber of the PTR (SC-PTR and AC-PTR) to increase the heat transfer performance. As stated in their studies, compared to the CSS-PTR, the maximum increase of the overall heat transfer performance factors for SC-PTR and AC-PTR were 135% and 148%, respectively. Cheng et al. (2012) placed longitudinal vortex generators on the bottom side of the absorber tube to improve the heat transfer without much pressure drop. The results showed that both the absorber wall temperature and the heat loss of the new PTR was decreased obviously. Huang et al. (2017) carried out a numerical study on the heat transfer performance of the dimpled PTRs at a fixed Reynolds number of 20000. It was revealed that as the Grashof number was in the range between 10^9 and 3.2×10^{10}, the Nusselt number and the friction factor of the deeply dimpled PTR (height=7 mm) increased by 1%~34% and 1%~21%, respectively, while those of shallow dimpled PTR (height=1 mm) increased by 1%~28% and 1%~18%, respectively. Zhu et al. (2017) designed a wavy-tape insert for enhancing the heat transfer inside the absorber tube. The simulation results indicated that, for the same pumping work, the wavy-tape insert not only reduced the heat loss and thermal stress, but also produced specific enthalpy gain of the fluid. Gong et al. (2017) added pin fin arrays on the bottom

side of the absorber tube to increase the heat transfer and decrease the circumferential temperature difference. The numerical results showed that the average Nusselt number rose by up to 9.0%, and the overall performance factor increased by 12%. Recently, Bitam et al. (2018) proposed a novel PTR with an S-curved/sinusoidal absorber tube. It is indicated that the average Nusselt number increased by 45%~63%, while the friction coefficient increased by less than 40.8%, which led to a maximum performance evaluation criteria of 135%. Bellos et al. (2018) investigated comprehensively the performance of a novel PTR with star shape insert in the absorber tube. The results were discussed in terms of thermal efficiency, exergy efficiency and collector efficiency. It was revealed that the drop of the heat loss was up to 14% and the pumping work was still extremely low (16 W) although the pressure drop was obvious. In another study of Bellos et al. (2017), the thermal performance of internally finned absorber was investigated. Twelve different fin geometries were examined under various operational conditions. It was obtained that the case with 20 mm length and 4 mm thickness was the optimum to achieve the highest thermal enhancement index.

It can be easily seen from the above literature review that installing inserts or modifying tube structure are effective ways to enhance the thermal performance of the PTR. Considering that the heat flux is mainly distributed on the part of the absorber facing to the reflector (i.e. the bottom arc), enhancing the heat transfer between the bottom inner surface of the absorber and the fluid will improve significantly the thermal performance of the PTR. Therefore, a novel absorber tube with spiral ribs laid on the

bottom inner surface was proposed in this study as the absorber of the PTR, named as unilateral spiral ribbed parabolic trough receiver (USR-PTR). Because of the disturbances and inducements of the spiral ribs, the boundary layer will be periodically destroyed and the secondary rotational flow will be triggered, which enhances the heat transfer of the PTR greatly. In addition, the discontinuous structure of the spiral rib can induce local longitudinal vortexes, further improving the heat transfer capacity. This study carried out a detailed numerical simulation on the thermal performance of the novel USR-PTR. The CFD simulation coupled with Monte Carlo Ray Tracing (MCRT) method was used to solve the optical-thermal coupled problem. The circumferential heat flux distribution calculated by the MCRT was loaded to the FLUENT code as the boundary condition using the User Defined Functions (UDF). A detailed comparison between the new USR-PTR and the original CSS-PTR was conducted in terms of both thermal and hydraulic performance. Moreover, the effects of the structural parameters of the spiral rib on the performance of the new PTR was further examined comprehensively.

2. Description of the USR-PTR

As shown in Fig. 1(a), the unilateral spiral ribbed parabolic trough receiver (USR-PTR) is designed by placing spiral ribs on the bottom half periphery of the absorber tube. This new absorber can be made by rolling the sheet metal with inclined rib stripes embossed on the surface into a tube. The major parameters of the USR-PTR, including the inner and outer diameters of the absorber and glass envelope ($d_{a,i}$, $d_{g,i}$, $d_{a,o}$, $d_{g,o}$,),

the rib pitch interval (p), the rib height (Δh), the rib crest radius (R_{cr}), the rib corner radius (R_{co}) and the spiral angle (α_s), are displayed in Fig. 1(b). Note that the conventional straight and smooth parabolic trough receiver (CSS-PTR) used for comparison in this study is the SEGS LS-2 PTR, which has been tested in the AZTRAK rotating platform by Sandia National Laboratories (Dudley et al., 1994). Thus, the diameters of the absorber and the glass envelope of the proposed USR-PTR are the same as that of the SEGS LS-2 PTR, the major parameters of which are presented in Table 1.

3. Modeling and validation

3.1 MCRT model

The circumferential heat flux distribution on the absorber outer surface will be calculated by the MCRT method, which is developed based on randomized trials and Ray Tracing Method (RTM). It initializes the position and the direction of the incident sunrays according to the sunshape model and determines the optical actions, including reflection, transmission and absorption, based on a series of randomly generated numbers. The propagating path of each ray is traced and the landing position on the absorber's outer surface is recorded accordingly to produce the statistical results of the heat flux distribution. For more detailed information about MCRT, please refers to the authors' previous study (Zou et al., 2017). The circumferential heat flux distribution on the absorber outer surface of the SEGS LS-2 PTR obtained by MCRT under ideal condition (without optical errors) is shown in Fig. 2.

3.2 Flow and heat transfer model

3.2.1 Governing equations

The governing equations of continuity, momentum and energy are given by Eq. (1) ~ Eq. (3) (Tao, 2001).

Continuity equation:

$$\frac{\partial(\rho u_i)}{\partial x_i} = 0 \tag{1}$$

Energy equation:

$$\frac{\partial(\rho c_p T u_i)}{\partial x_i} = \frac{\partial}{\partial x_i}\left[\left(\lambda + \frac{\mu_t}{\sigma_t}\right)\frac{\partial T}{\partial x_i}\right] \tag{2}$$

Momentum equation:

$$\frac{\partial(\rho u_i u_j)}{\partial x_j} = -\frac{\partial p}{\partial x_i} + \frac{\partial}{\partial x_j}\left[(\mu+\mu_t)\left(\frac{\partial u_i}{\partial x_j} + \frac{\partial u_j}{\partial x_i}\right) - \frac{2}{3}(\mu+\mu_t)\frac{\partial u_i}{\partial x_i}\delta_{ij} - \frac{2}{3}\rho k\delta_{ij}\right] + \rho F_i \tag{3}$$

The RNG k - ε model was adopted in this study to perform turbulence calculation, which can be given by Eq. (4) and Eq. (5).

k equation:

$$\frac{\partial(\rho k u_i)}{\partial x_i} = \frac{\partial}{\partial x_i}\left[\left(\mu + \frac{\mu_t}{\sigma_k}\right)\frac{\partial k}{\partial x_i}\right] + G_k - \rho\varepsilon \tag{4}$$

ε equation:

$$\frac{\partial(\rho \varepsilon u_i)}{\partial x_i} = \frac{\partial}{\partial x_i}\left[\left(\mu + \frac{\mu_t}{\sigma_\varepsilon}\right)\frac{\partial k}{\partial x_i}\right] + c_1\frac{\varepsilon}{k}G_k - c_2\rho\frac{\varepsilon^2}{k} - R_\varepsilon \tag{5}$$

The turbulence viscosity (μ_t) and the generation rate of k (G_k) are given by Eq. (6) and Eq. (7) respectively.

$$\mu_t = c_\mu \rho \frac{k^2}{\varepsilon} \tag{6}$$

$$G_k = \mu_t \frac{\partial u_i}{\partial x_j}\left(\frac{\partial u_i}{\partial x_j} + \frac{\partial u_j}{\partial x_i}\right) \tag{7}$$

The last term (R_ε) in ε equation is the modification of the standard k - ε model, which makes the model more accurate in simulating rotational flow, secondary flow and separation flow. It is calculated by Eq. (8).

$$R_\varepsilon = \frac{c_\mu \rho \eta^3 (1-\eta/4.38)}{1+0.012\eta^3}\frac{\varepsilon^2}{k} \tag{8}$$

where the time-average strain rate (η) is given by Eq. (9).

$$\eta = \frac{k}{\varepsilon}\sqrt{\frac{1}{2}\left(\frac{\partial u_i}{\partial x_j} + \frac{\partial u_j}{\partial x_i}\right)} \tag{9}$$

The constants in the turbulence model are listed in Table 2 (Tao, 2001).

3.2.2 Boundary conditions

The boundary conditions were set as following:

(1) Inlet: mass flow inlet, $\dot{m}_{in} = \dot{m}_z$, $\dot{m}_x = \dot{m}_y = 0$, $T=T_{in}$, $k_{in}=1\%\cdot 0.5\rho u_x^2$, $\varepsilon_{in}=c_\mu \rho k_{in}^2/\mu_t$ (Tao, 2001);

Outlet: outflow and fully developed assumption (Tao, 2001);

(2) All the receiver tube walls: No-slip boundary condition;

(3) The circumferential heat flux was calculated by the MCRT and loaded to the absorber outer surface using UDF; Fig. 3 shows the contour of the circumferential heat flux distribution on the absorber outer surface of the SEGS LS-2 PTR loaded by UDF. By comparing Fig. 2 and Fig. 3, it is clearly seen that the circumferential heat flux

distribution depicted in those two figures was the same, which demonstrates that the developed UDF program is accurate and reliable;

(4) The radiation between the absorber outer surface and the glass inner surface was calculated by the Surface to Surface (S2S) model;

(5) The outer surface of the glass envelope was set as mixed boundary condition including convection between the surface and the ambient, and radiation between the surface and the sky. The heat transfer coefficient between the glass envelope outer surface and the ambient was calculated by Eq. (10) (Mullick, 1989), and the sky temperature was viewed as 8 K lower than the ambient temperature (Forristall, 2003). The emittance of the glass envelope was 0.86, and that of the selective absorbing coating (Cermet) was given by Eq. (11) (Forristall, 2003).

$$h_{g-amb} = 4v_{amb}^{0.58} d_{g,o}^{-0.42} \tag{10}$$

$$\varepsilon_{coa} = 0.000327 \times T - 0.065971 \tag{11}$$

3.2.3 Solution method

The flow and heat transfer simulation was conducted using the FLUENT codes which were developed based on the Finite Volume Method (FVM). A UDF program developed for describing the heat flux distribution calculated by the MCRT was read by the FLUENT as the boundary condition of the absorber outer surface. The SIMPLE algorithm was adopted to treat the coupling of pressure and velocity. The governing equations were discretized by second order upwind scheme. Given that the k - ε turbulence model is not applicable in the vicinity of the pipe wall, the enhanced wall

treatment was used to deal with the flow and heat transfer close to the solid walls. Two criteria were used to guarantee the convergence of the solution: the maximum residual for all the equations were less than 10^{-6}, and the outlet temperature of the fluid maintained constant for the last 1000 iterations.

3.2.4 Definition of performance parameters

In this part, several important parameters that will be used to evaluate the performance of the PTR are given and defined clearly.

The useful energy (q_u) obtained by the fluid is calculated by:

$$q_u = m\left(c_{p,out}T_{out} - c_{p,in}T_{in}\right) \tag{12}$$

The mean Nusselt number (Nu) is calculated by:

$$Nu = \frac{q_u}{A_{a,i}\left(T_{a,i} - T_f\right)} \times \frac{d_{a,i}}{\lambda} \tag{13}$$

The mean fluid temperature is given by:

$$T_f = \frac{T_{in} + T_{out}}{2} \tag{14}$$

The mean friction factor (f) is given by:

$$f = \frac{2\Delta P}{\rho v^2}\left(\frac{d_{a,i}}{L_a}\right) \tag{15}$$

Generally, the CSS-PTR is usually used as the reference for assessing the performance of a PTR with new structure. Nu/Nu_0 and f/f_0 are used for evaluation of the heat transfer performance and pressure drop property respectively. A performance evaluation criterion (PEC) which takes into account both the heat transfer enhancement and the pressure drop penalty is given by Eq. (16) (Hasanpour et al., 2014). The PEC

compares the heat transfer capacity between the new PTR and the CSS-PTR with the same pumping work, which can be used as the overall performance factor of the new PTR. When the PEC is more than 1, the overall performance of the new PTR is better than that of the CSS-PTR, otherwise poorer.

$$\mathrm{PEC} = \frac{\left(Nu / Nu_0\right)}{\left(f / f_0\right)^{1/3}} \tag{16}$$

3.3 Grid independence checking and model validation

The heat transfer fluid (HTF) used in this study was Syltherm 800, the thermophysical parameters of which were temperature dependent and given in Table 3 (Agustin et al., 2007).

3.3.1 Grid independence checking

The purpose of grid independence checking is to find the minimum number of grids ensuring the accuracy of the results. Given the relatively complex internal structure of the USR-PTR, unstructured grids were utilized in this study, and the total number of the cells in the grid was determined by setting respectively the size of the cells in each computational domain. The outlet temperature of the fluid (T_{out}), the mean Nusselt number (Nu) and the mean friction factor (f) are used for grid independence checking. The structural parameters of the USR-PTR used for grid independence checking was listed in Table 4. The mass flow rate was 2 kg/s and the inlet fluid temperature was 573.15 K. For simplification, this study adopted the receiver tube with the length of one meter as the research object. The results for grid independence checking is shown in Table 5. It can be seen from Table 5 that when the number of grids

was more than 1130000, the results of T_{out}, Nu and f all changed very little. Therefore, the grid system with 1130000 cells was used in this study. The schematic of domain discretization (meshing) of the receiver tube is shown in Fig. 4.

3.3.2 Model validation

Six typical cases were selected from Sandia test (Dudley et al., 1994) for validation purpose, which were given in Table 6. The established models will be validated by comparing the simulated fluid outlet temperature ($T_{out,s}$) with the tested fluid outlet temperature ($T_{out,t}$). The relative error (e_T) is defined by Eq. (17).

$$e_T = \frac{\left|T_{out,s} - T_{out,t}\right|}{\left|T_{out,t} - T_{in}\right|} \times 100\% \tag{17}$$

The comparison of the simulation and test results is given in Table 7. It can be seen from Table 7 that the simulation results agreed well with the test results. The maximum relative error of the outlet temperature was 10.23% and the average relative error was about 8.75%, demonstrating that the established models are reliable for simulating the actual flow and heat transfer process of the PTR.

In Sandia test, a solid plug was inserted concentrically in the absorber tube to ensure relatively large velocity. Whereas, in this study, a totally hollow absorber tube (i.e. solid plug removed) will be used. Therefore, in order to further validate the applicability of the established models in simulation of flow and heat transfer in the hollow tube, the obtained results of Nu and f were compared with that calculated by the classical empirical formulas proposed by Gnielinski (1976) and Petukhov (1970). The two empirical formulas were given by Eq. (18) and Eq. (19) respectively.

$$Nu_G = \frac{(f/8)(Re-1000)Pr_f}{1+12.7(f/8)^{1/2}\left(Pr_f^{2/3}-1\right)}\left[1+\left(\frac{d_{a,i}}{L_a}\right)^{2/3}\right]\left(\frac{Pr_f}{Pr_{a,i}}\right)^{0.11} \quad (18)$$

$$f_P = \left[1.82\log(Re)-1.64\right]^{-2} \quad (19)$$

The comparison of the results between simulation and empirical formulas was shown in Fig. 5. It is clearly seen from the figure that the simulation results were in good accordance with the results calculated by the empirical formulas. As the mass flow rate increased from 0.5 kg/s to 3.5 kg/s, the maximum relative error of Nu and f was 5.13% and 9.34% respectively, and the average relative error was only 4.25% and 2.88% respectively, validating the reliability of the established models.

4. Results and discussion

The study was performed under the following conditions: the length of the PTR was 1 m; the incident solar radiation intensity was 1000 W/m^2; the ambient temperature was 293.15 K; the wind velocity was 2 m/s; the inlet temperature of the fluid was 573.15 K; the mass flow rate ranged from 0.5 kg/s to 3.5 kg/s. The inlet Reynolds number corresponding to each mass flow rate was listed in Table 8.

4.1 Comparison of USR-PTR and CSS-PTR

In this section, the USR-PTR and the CSS-PTR were compared in terms of both thermal and hydraulic performance, aiming at revealing the mechanism of the heat transfer enhancement in the USR-PTR. The CSS-PTR used as the reference was the SEGS LS-2 PTR, the major parameters of which was given in Table 1. The rib parameters of the USR-PTR used for comparison in this section was given in Table 4. The other parameters, such as absorber diameter, glass envelope diameter, are the same

as the SEGS LS-2 PTR. The mass flow rate of 2 kg/s and a periodic length of the PTR from z=600 mm to z=700 mm were selected as representation for detailed analysis.

4.1.1 Comparison of thermal performance

Fig. 6 shows the variation of the Nusselt number (*Nu*) with the mass flow rate ($\dot{m}$) for both USR-PTR and CSS-PTR. It is clearly seen from the figure that *Nu* increased almost linearly with the increase of $\dot{m}$ for both the two PTRs. The *Nu* and its growth rate of the USR-PTR were both obviously larger than those of the CSS-PTR. When the $\dot{m}$ increased from 0.5 kg/s to 3.5 kg/s, the *Nu* of the CSS-PTR grew from 217 to 916, rising by 3.22 times, whereas the *Nu* of the USR-PTR increased greatly from 312 to 1598, growing by 4.12 times. It can be calculated form Fig. 6 that the heat transfer enhancement of the USR-PTR, compared with the CSS-PTR, ranged from 44% to 76%. This indicates that the USR-PTR has great capacity of improving the heat transfer of the PTR.

Fig. 7 shows the fluid temperature distribution in the longitudinal section from z=600 mm to z=700 mm under condition of $\dot{m}$=2 kg/s for both USR-PTR and CSS-PTR. Overall, the fluid temperature in the USR-PTR was higher and more uniform than that in the CSS-PTR. This is because the larger turbulence caused in the USR-PTR enhances the heat transfer of the fluid. There existed a thermal boundary layer in the vicinity of the bottom inner surface of the absorber, which causes the major resistance of the heat transfer between the absorber and the fluid. It can be clearly seen from Fig. 7 that the thermal boundary layer of the USR-PTR was much thinner than that of the

CSS-PTR, leading to smaller thermal resistance and hence producing larger heat transfer ability. For more clarity, a local enlarged view was given in Fig. 7(b). It can be seen from the enlarged view that the thermal boundary layer was thickened along the flow direction and peaked at the upstream of the rib, and then was reduced obviously after the rib. The possible reason is that the disturbance (even vortexes) caused by the rib destroys the boundary layer. This periodic disturbance inhibits the development of the boundary layer, reducing effectively the thermal resistance and hence improving the heat transfer.

Fig. 8 presents the absorber temperature distribution from z=600 mm to z=700 mm under condition of $\dot{m}$ =2 kg/s for both USR-PTR and CSS-PTR. It is obviously observed from the figure that the temperature of the bottom part of the absorber of the USR-PTR was smaller than that of the CSS-PTR. That means the circumferential temperature difference of the USR-PTR will be smaller than that of the CSS-PTR, reducing the thermal strain and hence improving the safety of the PTR. Fig. 8 also shows that the temperature of the absorber outer surface was higher than that of the inner surface. This is because the solar radiation impinges on the outer surface of the absorber. Taking the cross-section of z=600 mm as an example, the variation of the maximum ($T_{a,max}$) and minimum ($T_{a,min}$) temperature of the absorber with mass flow rate ($\dot{m}$) is shown in Fig. 9. It can be found from the figure that the $T_{a,min}$ for the two PTRs were almost the same, while the $T_{a,max}$ of the USR-PTR was consistently smaller than that of the CSS-PTR for all the discussed mass flow rates. Accordingly, the

maximum circumferential temperature difference of the absorber of the USR-PTR will be smaller than that of the CSS-PTR. For example, when $\dot{m}$ =2 kg/s, the maximum circumferential temperature difference of the CSS-PTR was about 59.5 K, while that of the USR-PTR was only about 46.6 K, 21.7% smaller than the former. As a matter of fact, compared to the CSS-PTR, the maximum decrease of the circumferential temperature difference of the USR-PTR was up to 25% which was obtained for $\dot{m}$ =3.5 kg/s. It can be concluded from the above analysis that the security and stability of the PTR will be improved by using the USR-PTR, especially in the cases of larger flow rates.

4.1.2 Comparison of hydraulic performance

Fig. 10 depicts the variation of the pressure drop (ΔP) with mass flow rate ($\dot{m}$) for both USR-PTR and CSS-PTR. It is clear that the ΔP increased constantly with the increase of $\dot{m}$ for both the two PTRs. The ΔP and its growth rate for the USR-PTR were much larger than those for the CSS-PTR. As the *m* increased from 0.5 kg/s to 3.5 kg/s, the ΔP for the CSS-PTR increased from 8.7 Pa to 236.1 Pa, rising by 26.1 times, whereas the ΔP for the USR-PTR grew greatly from 26.5 Pa to 1098.9 Pa, increasing by 40.5 times. This indicates that the USR-PTR enhances the heat transfer at the expense of increasing the pressure drop penalty. The comparison of the friction factor (*f*) between the two PTRs are presented in Fig. 11. It shows clearly that the value of *f* of the USR-PTR was much larger than that of the CSS-PTR. For example, the value of *f* of the USR-PTR in the case of $\dot{m}$ =2 kg/s was about 0.0884, 4.09 times larger than

that of the CSS-PTR, which was only 0.0216. It can also be found from Fig. 11 that the f decreased with the increase of $\dot{m}$, indicating that, according to Eq. (15), the growth rate of the ΔP is smaller than that of the kinetic energy with the increase of flow rate.

Fig. 12 shows the fluid velocity vector distribution in the longitudinal section from z=600 mm to z=700 mm under condition of $\dot{m}$=2 kg/s for both USR-PTR and CSS-PTR. Obviously, the velocity vectors in the CSS-PTR were parallel, whereas those in the USR-PTR interblent with each other, especially in the near-wall region. It can be seen from the local enlarged view in the figure that, compared to the CSS-PTR, counter-flow was induced at the back of the rib in the USR-PTR, forming a recirculation zone. The velocity vectors were separated in the recirculation zone and then adhered again to the wall in the downstream region, which is very beneficial for breaking the boundary layer and hence reducing the thermal resistance. It can also be found from Fig. 12(b) that, although the spiral ribs were only placed on the bottom surface of the absorber, the caused turbulence also affected remarkably the fluid flowing in the upper region of the absorber. In order to further explore the flow properties in the USR-PTR, the velocity vectors in four typical cross sections in one periodic tube length are depicted in Fig. 13. It is obviously seen from the figure that the rotational flow was induced in the cross section of the USR-PTR, which will enhance fluid mixing and disturbance, consequently improving the heat transfer performance. From the Fig. 13, we can also find that three longitudinal vortexes were generated in each cross section, which will further increase the disturbance of the fluid and enhance the heat transfer in the tube.

What is noted is that the greater turbulence in the USR-PTR is also the major cause of the larger pressure drop than the CSS-PTR (as shown in Fig. 10).

Fig. 14 depicts the distribution of the turbulent kinetic energy (TKE) in the longitudinal section from z=600 mm to z=700 mm under condition of $\dot{m}$ =2 kg/s for both USR-PTR and CSS-PTR. It can be easily seen from the figure that the TKE in the USR-PTR was much larger than that in the CSS-PTR. The TKE in most regions of the CSS-PTR was less than 0.002 m^2/s^2, while that in the whole USR-PTR was more than 0.004 m^2/s^2. The maximum TKE in the CSS-PTR was less than 0.01 m^2/s^2, while that in the USR-PTR was more than 0.02 m^2/s^2. This demonstrates that the fluid in the USR-PTR is mixed more drastically than in the CSS-PTR, hence enhancing the heat transfer ability and increasing the pressure loss as well. Fig. 14 also shows that, in the USR-PTR, the maximum TKE occurred after fluid flowing over the rib because of the great disturbance and vortexes caused by the rib. The maximum TKE was close to the absorber inner surface, which can reduce the boundary layer and decrease the thermal resistance. It can be seen from the two local enlarged views that there existed a thin layer of fluid with extremely small TKE (≈0) near the absorber inner surface. This is because the viscosity of the fluid dominates in the near-wall region, reducing the TKE remarkably. From the figure, it can also be found that the flow layer with small TKE in the USR-PTR was thinner than that in the CSS-PTR, indicating that the thermal resistance in the USR-PTR is reduced effectively. Fig. 14(b) also shows that the TKE of the fluid in the upper region of the absorber of the USR-PTR was larger than that in

the central region. This is caused by the rotational flow induced by the spiral ribs.

4.2 Influences of structural parameters of the rib

In this section, the influences of the structural parameters of the rib, including the pitch interval, the rib height, the corner radius and the spiral angle, on the performance of the USR-PTR were discussed in detail. Four or five different values were set for each structural parameter, while other parameters remained the same as those given in Table 4. The parameters of the CSS-PTR with a subscript of "0" were used as the reference, and the performance of the USR-PTR was represented by the ratio to the CSS-PTR (i.e. Nu/Nu_0 and f/f_0). The PEC was used to evaluate the overall performance of the USR-PTR.

4.2.1 Influences of the pitch interval of the rib

Fig. 15 shows the variation of Nu/Nu_0 with mass flow rate ($\dot{m}$) under different pitch intervals (p). It is clearly seen from the figure that Nu/Nu_0 for all p first increased quickly, and then declined slowly with the increase of $\dot{m}$. That is to say, there is an optimal flow rate range within which the USR-PTR can achieve the maximum heat transfer enhancement. As p increased, Nu/Nu_0 was reduced. This is because larger p cuts down the number of the ribs in a certain length of tube, reducing the disturbance frequency and hence weakening the heat transfer. The maximum Nu/Nu_0 was obtained for p=50 mm in the case of $\dot{m}$=2.5 kg/s, which was about 1.805. This means that, compared with the CSS-PTR, the enhancement of the heat transfer of the USR-PTR can be up to 80.5% by changing the pitch interval of the rib (p).

Fig. 16 shows the variation of f/f_0 with mass flow rate ($\dot{m}$) under different pitch intervals (p). Obviously, f/f_0 for all p first increased, and then declined slightly with the increase of $\dot{m}$. Since both the disturbance frequency and constraint effect are weakened by increasing p, f/f_0 decreased constantly with the increase of p. The maximum f/f_0 was about 4.97 obtained for p=50 mm in the case of $\dot{m}$ =3 kg/s, indicating that the pressure drop will be increased by up to 3.97 times by decreasing the pitch interval of the rib (p).

Fig. 17 presents the variation of PEC with mass flow rate ($\dot{m}$) under different pitch intervals (p). It is clearly seen that PEC first increased, and then decreased slowly with the increase of $\dot{m}$. The $\dot{m}$ that achieves the maximum PEC varied with p, which means that the optimum flow rate for the best overall performance is closely associated with the pitch interval. When $\dot{m}$ was less than 0.75 kg/s, the overall performance of the USR-PTR with p larger than 100 mm is not so good as the CSS-PTR (PEC<1), demonstrating that the USR-PTR is not very suitable for application in the case of small flow rate. The figure also shows that when $\dot{m}$ was less than 1 kg/s, the PEC decreased with increasing p, while increased with increasing p as $\dot{m}$ was more than 2.5 kg/s. Therefore, the USR-PTRs with larger pitch interval have greater advantages when applied under condition of large flow rates. The maximum PEC was 1.125 obtained for p=200 mm at $\dot{m}$ =3 kg/s, indicating that the overall performance of the USR-PTR can be improved by 12.5% compared with the CSS-PTR by changing the pitch interval of the rib (p).

4.2.2 Influences of the height of the rib

Fig. 18 shows the variation of Nu/Nu_0 with mass flow rate ($\dot{m}$) under different rib heights (Δh). It is easily observed from the figure that Nu/Nu_0 for all Δh first increased quickly, and then dropped slowly with the increase of $\dot{m}$. The heat transfer enhancement was more obvious as the flow rate was more than 1.5 kg/s. The figure also shows that Nu/Nu_0 increased constantly with the increase of Δh. This is because larger Δh increased the disturbance intensity of the fluid, which enhances fluid mixing and weakens the boundary layer, hence improving the heat transfer. The increase of Nu/Nu_0 with increasing Δh was diminished, indicating that the heat transfer enhancement by increasing continuously rib height is limited. The maximum Nu/Nu_0 was achieved for Δh=9 mm in the case of $\dot{m}$ =2.5 kg/s, which was about 1.963. This means that, compared with the CSS-PTR, the heat transfer of the USR-PTR can be augmented by up to 96.3% by increasing the rib height (Δh).

Fig. 19 shows the variation of f/f_0 with mass flow rate ($\dot{m}$) under different rib heights (Δh). Clearly, f/f_0 for all Δh increased slightly with the increase of $\dot{m}$, indicating that the increase of pressure loss of the USR-PTR is almost the same as that of the CSS-PTR under conditions of different flow rates. For any $\dot{m}$, f/f_0 increased obviously with the increase of Δh. This is because the disturbance and constraint enhanced by increasing rib height increase the energy dissipation and flow resistance. It can also be found from the figure that the maximum f/f_0 was about 6.1 obtained for Δh=9 mm in the case of $\dot{m}$ =3.5 kg/s, indicating that the increase of pressure loss of

the USR-PTR will be up to 5.1 times that of the CSS-PTR by increasing the rib height (Δh).

Fig. 20 presents the variation of PEC with mass flow rate ($\dot{m}$) under different rib heights (Δh). It is clearly seen that PEC first increased quickly, and then decreased slowly with the increase of $\dot{m}$. The overall performance of the USR-PTR is more susceptible to flow regime under conditions of small flow rates. The figure also shows that when $\dot{m}$ was 0.5 kg/s, PEC for all the discussed Δh were less than 1, indicating that the overall performance of the USR-PTR is inferior to the CSS-PTR under conditions of small flow rates. When applied in cases of relatively larger flow rates, the advantage of the USR-PTR in improving the overall performance is more obvious. It can also be found from the figure that PEC decreased with the increase of Δh. This demonstrates that the growing rate of the heat transfer enhancement with increasing rib height is smaller than that of the increase of pressure loss. Therefore, in view of the overall performance, the USR-PTR with relatively small rib height is more applicable in practice. The maximum PEC was 1.098 obtained for Δh=3 mm at $\dot{m}$ =2 kg/s, indicating that the overall performance of the USR-PTR can be improved by up to 9.8% compared with the CSS-PTR by changing the rib height (Δh).

4.2.3 Influences of the corner radius of the rib

Fig. 21 shows the variation of Nu/Nu_0 with mass flow rate ($\dot{m}$) under different corner radiuses (R_{co}). It is clearly seen from the figure that for all R_{co} first increased quickly, and then declined slowly with the increase of $\dot{m}$. In addition, the Nu/Nu_0 under

large flow rates was larger and more stable than that under small flow rates, indicating that the USR-PTR is more suitable for situations with larger flow rate. It can also be found that Nu/Nu_0 decreased consistently with the increase of R_{co}. The reason is that when R_{co} is increased, the edges of the rib become more flat and smooth, allowing the fluid flowing more gently over the rib, thereby reducing the disturbance intensity and weakening the heat transfer. The maximum Nu/Nu_0 was 1.76 achieved for R_{co}=5 mm in the case of $\dot{m}$ =2.5 kg/s, which means that, compared with the CSS-PTR, the heat transfer of the USR-PTR can be enhanced by up to 76% by reducing the corner radius (R_{co}).

Fig. 22 shows the variation of f/f_0 with mass flow rate ($\dot{m}$) under different corner radiuses (R_{co}). Obviously, the variation curve of f/f_0 for all R_{co} first increased with the increase of $\dot{m}$, and then became flat. This demonstrates that the increase of pressure loss of the USR-PTR is getting closer to that of the CSS-PTR with the increase of flow rate. For any $\dot{m}$, f/f_0 decreased constantly with the increase of R_{co}. This is because increasing corner radius makes the rib edge more flat and smooth, hence reducing the flow resistance. The maximum f/f_0 was about 4.33 obtained for R_{co}=5 mm in the case of $\dot{m}$ =3.5 kg/s, indicating that the pressure drop of the USR-PTR can be up to 4.33 times that of the CSS-PTR by decreasing the corner radius (R_{co}).

Fig. 23 presents the variation of PEC with mass flow rate ($\dot{m}$) under different corner radiuses (R_{co}). It is clearly seen from the figure that PEC first increased quickly and then maintained slow growth, and finally decreased with the increase of $\dot{m}$. When

$\dot{m}$ was 0.5 kg/s, the PEC for R_{co}=5 mm, R_{co}=10 mm and R_{co}=15 mm were less than 1, which means that the overall performance of the USR-PTR is poorer as the CSS-PTR in those cases. The overall performance of the USR-PTR was much better under conditions of larger flow rate ($\dot{m}$ >1 kg/s). It can also be found from the figure that PEC increased continuously with the increase of R_{co}. This demonstrates that the drop rate of the increase of pressure loss with increasing corner radius is larger than that of the heat transfer enhancement. Therefore, increasing the corner radius is an effective way to improve the overall performance of the USR-PTR. The maximum PEC was 1.108 obtained for R_{co}=20 mm at $\dot{m}$ =2.5 kg/s, indicating that the overall performance of the USR-PTR can be improved by up to 10.8% compared with the CSS-PTR by increasing the corner radius of the rib (R_{co}).

4.2.4 Influences of the spiral angle of the rib

Fig. 24 shows the variation of Nu/Nu_0 with mass flow rate ($\dot{m}$) under different spiral angles (α_s). It can be clearly seen from the figure that Nu/Nu_0 for all α_s first increased, and then decreased slowly with the increase of $\dot{m}$. Overall, the heat transfer enhancement of USR-PTR is more obvious under conditions of large flow rates. It can also be found from Fig. 24 that Nu/Nu_0 first increased and then declined with the increase of α_s. Take $\dot{m}$ =2 kg/s as an example, the Nu/Nu_0 for α_s=15°, α_s=30°, α_s=45°, α_s=60° and α_s=75° was 1.272, 1.648, 1.699, 1.738 and 1.522 respectively. Obviously, α_s=60° is the spiral angle that achieves the maximum heat transfer enhancement among the five discussed spiral angles. The maximum Nu/Nu_0 was 1.76 achieved for α_s=60°

in the case of $\dot{m}$ =2.5 kg/s, which indicates that, compared with the CSS-PTR, the heat transfer of the USR-PTR can be augmented by up to 76% by changing the spiral angle (α_s).

Fig. 25 shows the variation of f/f_0 with mass flow rate ($\dot{m}$) under different spiral angles (α_s). It can be seen from the figure that f/f_0 for most R_{co} increased with the increase of $\dot{m}$, and the growth rate increased with the increase of R_{co}. This means that the pressure loss is more easily affected by the flow rate in the cases of larger spiral angles. For any $\dot{m}$, f/f_0 increased constantly with the increase of R_{co}. The main reason is that the constraint effect of the ribs are enhanced by increasing the spiral angle, consequently increasing the flow resistance. The maximum f/f_0 was about 5.51 obtained for α_s=75° in the case of $\dot{m}$ =3.5 kg/s, indicating that the pressure drop of the USR-PTR can be increased by up to 4.51 times that of the CSS-PTR by increasing the spiral angle (α_s).

Fig. 26 presents the variation of PEC with mass flow rate ($\dot{m}$) under different spiral angles (α_s). It is easily seen from the figure that the PEC for α_s=75° was smaller than 1 in the discussed flow rate range, revealing that the overall performance of the USR-PTR is always poorer than that of the CSS-PTR in this case. Thus, the spiral angle of the rib should not be too large in practical application. PEC for other four spiral angles first increased quickly and then varied slightly with the increase of $\dot{m}$. This demonstrates that the overall performance enhancement of the USR-PTR is more obvious and stable under condition of large flow rates. The figure also shows that the

PEC first increased and then decreased with the increase of α_s. It is easily found from the figure that α_s=30° is the optimum among the five discussed spiral angles that produces the maximum overall performance for the USR-PTR. Therefore, in view of overall performance, the spiral angle of 30° is the most advisable for structural design. The maximum PEC was 1.301 obtained for α_s=30° at $\dot{m}$ =2.5 kg/s, which demonstrates that, compared with the CSS-PTR, the overall performance of the USR-PTR can be improved by up to 30.1% by changing the spiral angle of the rib (α_s).

5. Conclusions

A novel unilateral spiral ribbed receiver tube (USR-PTR) for improving the thermal performance of PTC was proposed in this study. Detailed numerical study on the thermo-hydraulic performance of the USR-PTR was carried out using the CFD tool coupled with MCRT method. A comprehensive comparison between the USR-PTR and the CSS-PTR was conducted, revealing the mechanism and benefit of the USR-PTR in thermal enhancement. The influences of the structural parameters of the spiral rib on the performance of the USR-PTR were further investigated in detail. Some important conclusions can be drawn as follows:

(1) Fluid disturbance, secondary rotational flow and local longitudinal vortexes induced by the discontinuous spiral ribs are the three main causes of heat transfer enhancement in the USR-PTR. The USR-PTR enhances the heat transfer capacity at the expense of increasing obviously the pressure loss. The temperature on the absorber wall is more uniform and the circumferential temperature difference is reduced

effectively by using the USR-PTR. For the structure discussed in the study, the circumferential temperature difference of the USR-PTR is reduced at most by 25% to the CSS-PTR. The advantage of the USR-PTR in improving the overall performance of the PTR is more obvious in the cases of large flow rates. In practice, the USR-PTR should be applied in cases of relatively large flow rates ($\dot{m}$ >1.25 kg/s).

(2) Both heat transfer and pressure loss increase with reducing the rib pitch interval or increasing the rib height or reducing the corner radius. When the mass flow rates is larger than 2.5 kg/s, the overall performance of the USR-PTR is enhanced by increasing the rib pitch interval, while weakened by increasing the rib pitch as the mass flow rate is less than 1 kg/s. Within the discussed flow rate range, the overall performance of the USR-PTR is improved constantly by decreasing the rib height or increasing the corner radius. The maximum improvement of the overall performance of the USR-PTR, compared with the CSS-PTR, by setting individually the pitch interval, the rib height and the corner radius is 12.5%, 9.8% and 10.8% respectively.

(3) With the increase of the rib spiral angle, the heat transfer increases first and then declines, while the pressure loss increases continuously. The pressure loss is more sensitive to the flow rate under the condition of larger spiral angles. Among the five discussed spiral angles, the optimal one to achieve the maximum overall performance for the USR-PTR is 30°. Compared with the CSS-PTR, the overall performance of the USR-PTR can be improved by up to 30.1% by using the optimal spiral angle.

This study mainly focused on the thermal enhancement mechanism and the

influences of single structural parameter on the performance of the USR-PTR. The next work will conduct a parametric optimization for the USR-PTR, taking into account simultaneously the coupling effects of all the parameters.

Acknowledgements

This work was supported by the National Key R&D Program of China (Project Number: 2017YF0702604).

References

Agustin, MD-T., Lourdes, G.R., 2007. Comparison of solar technologies for driving a desalination system by means of an Organic Rankine Cycle. Desalination 216, 276-291.

Almanza, R., Jmenez, A.L.G., 1997. Receiver behavior in direct steam generation with parabolic troughs. Solar Energy 4, 275-278.

Bellos, E., Tzivanidis, C., 2018. Investigation of a star flow insert in a parabolic trough solar collector. Applied Energy 224, 86-102.

Bellos, E., Tzivanidis, C., Tsimpoukis, D., 2017. Thermal enhancement of parabolic trough collector with internally finned absorbers. Solar Energy 157, 514-531.

Benoit, H., Spreafico, L., Gauthier, D., Flamant, G., 2016. Review of heat transfer fluids in tube-receivers used in concentrating solar thermal systems: properties and heat transfer coefficients. Renewable and Sustainable Energy Reviews 55, 298-315.

Bermejo. P., Pino, F.J., Rosa, F., 2010. Solar absorption cooling plant in Seville. Solar Energy 84, 1503-1512.

Bitam, E.W., Demagh, Y., Hachicha, A.A., Benmoussa, H., Kabar, Y., 2018. Numerical investigation of a novel sinusoidal tube receiver for parabolic trough technology. Applied Energy 218, 494-510.

Cabrera, F.J., Fernandez-Garcia, A., Silva R.M.P., Perez-Garcia M., 2013. Use of parabolic trough solar collectors for solar refrigeration and air-conditioning applications. Renewable and Sustainable Energy Reviews 20, 103-118.

Cheng, Z.D., He, Y.L., Cui, F.Q., 2012. Numerical study of heat transfer enhancement by unilateral longitudinal vortex generators inside parabolic trough solar receivers. International Journal of Heat and Mass Transfer 55, 5631-5641.

Conrado, L.S., Rodriguez-Pulido, A., Calderon, G., 2017. Thermal performance of parabolic trough solar collectors. Renewable and Sustainable Energy Reviews 67, 1345-1359.

Devabhaktuni, V., Alam, M., Depuru, S.S.S.R., Green-II, R.C., et al., 2013. Solar energy: Trends and enabling technologies. Renewable and Sustainable Energy Reviews 19, 555-564.

Dudley, V., Kolb, G., Sloan, M., Kearney, D., 1994. SEGS LS2 solar collector–test results. Report of Sandia National Laboratories, Albuquerque, NM, USA; SANDIA 94-1884.

Fernandez-Garcia, A., Zarza, E., Valenzuela, L., Perez, M., 2010. Parabolic-trough solar collectors and their applications. Renewable and Sustainable Energy Reviews 14, 1695-1721.

Forristall, R., 2003. Heat transfer analysis and modeling of a parabolic trough solar receiver implemented in Engineering Equation Solver. NREL/TP-550-34169.

Ghadirijafarbeigloo, S., Zamzamian, A.H., Yaghoubi, M., 2014. 3-D numerical simulation of heat transfer and turbulent flow in a receiver tube of solar parabolic trough concentrator with louvered twisted-tape inserts. Energy Procedia, 49, 373-380.

Gnielinski V., 1976. New equations for heat and mass transfer in turbulent pipe and channel flow. International Chemical Engineering 16, 359-368.

Gong, X., Wang, F., Wang, H., Tan, J., Lai, Q., Han, H., 2017. Heat transfer enhancement analysis of tube receiver for parabolic trough solar collector with pin fin arrays inserting. Solar Energy 144, 185-202.

Hasanpour, A., Farhadi, M., Sedighi, K., 2014. A review study on twisted tape inserts on turbulent flow heat exchangers: the overall enhancement ratio criteria. International Communications in Heat and Mass Transfer 55, 53-62.

Huang, Z., Li, Z.Y., Yu, G.L., Tao, W.Q., 2017. Numerical investigations on fully-developed mixed turbulent convection in dimpled parabolic trough receiver tubes. Applied Thermal Engineering 114, 1287-1299.

Jebasingh, V.K., Joselin-Herbert, G.M., 2016. A review of solar parabolic trough collector. Renewable and Sustainable Energy Reviews 54, 1085-1091.

Kalidasan, B., Shankar, R., Srinivas, T., 2016. Absorber tube with internal hinged blades for solar parabolic trough collector. Energy Procedia 90, 463-469.

Kalogirou, S.A., 1998. Use of parabolic trough solar energy collectors for sea-water desalination. Applied Energy 60, 65-88.

Kalogirou, S.A., 2002. Parabolic trough collectors for industrial process heat in Cyprus. Energy 27, 813-830.

Kalogirou, S.A., 2003. Solar thermal collectors and applications. Progress in Energy and Combustion Science 30, 231-295.

Khanna, S., Kedare, S.B., Singh, S., 2014. Deflection and stresses in absorber tube of solar parabolic trough due to circumferential and axial flux variations on absorber tube supported at multiple points. Solar Energy 99, 134-151.

Kumar, K.R., Reddy, K.S., 2009. Thermal analysis of solar parabolic trough with porous disc receiver. Applied Energy 86, 1804-1812.

Mills, D., 2004. Advances in solar thermal electricity technology. Solar Energy 76, 19-31.

Mullick, S.C., Nanda, S.K., 1989. An improved technique for computing the heat loss factor of a tubular absorber. Solar Energy 42, 1-7.

Munoz, J., Abanades, A., 2011. Analysis of internal helically finned tubes for parabolic trough design by CFD tool. Applied Energy 88, 4139-4149.

Mwesigye, A., Bello-Ochende, T., Meyer, J.P., 2014. Heat transfer and thermodynamic performance of a parabolic trough receiver with centrally placed perforated plate inserts. Applied Energy 136, 989-1003.

Petukhov BS. 1970. Heat Transfer and Friction in Turbulent Pipe Flow with Variable

Physical Properties. Advances in Heat Transfer 6, 503-564.

Reddy, K.S., Kumar, K.R., Ajay, C.S., 2015. Experimental investigation of porous disc enhanced receiver for solar parabolic trough collector. Renewable Energy 77, 308-319.

Sandeep, H.M., Arunachala, U.C., 2017. Solar parabolic trough collectors: A review on heat transfer augmentation techniques. Renewable and Sustainable Energy Reviews 69, 1218-1231.

Scrivani, A, Asmar, T.E., Bardi. U., 2007. Solar trough concentration for fresh water production and waste treatment. Desalination 206, 485-493.

Tao, W.Q., 2001. Numerical Heat Transfer (2nd Edition). Xi'an Jiaotong University Press, Xi'an.

Wang, F.Q., Cheng, Z.M., Tan, J.Y., Yuan, Y., et al. 2017. Progress in concentrated solar power technology with parabolic trough collector system: A comprehensive review. Renewable and Sustainable Energy Reviews 79, 1314-1328.

Wang, F.Q., Lai, Q.Z., Han, H.Z., Tan, J.Y., 2016. Parabolic trough receiver with corrugated tube for improving heat transfer and thermal deformation characteristics. Applied Energy 164, 411-424.

Wang, F.Q., Tang, Z.X., Gong, X.T., Tan, J.Y., Han, H.Z., Li, B.X., 2016. Heat transfer performance enhancement and thermal strain restrain of tube receiver for parabolic trough solar collector by using asymmetric outward convex corrugated tube. Energy 114, 275-292.

Wang, P., Liu, D.Y., Xu, C., 2013. Numerical study of heat transfer enhancement in the receiver tube of direct steam generation with parabolic trough by inserting mental foams. Applied Energy 102, 449-460.

Wang, Z.Y., Yang, W.S., Qiu, F., Zhang Z.M., Zhao X.D., 2015. Solar water heating: From theory, application, marketing and research. Renewable and Sustainable Energy Reviews 41, 68-84.

Xu, X.H., Vignarooban, K., Xu, B., Hsu K., Kannan, A.M., 2016. Prospects and problems of concentrating solar power technologies for power generation in the desert regions. Renewable and Sustainable Energy Reviews 53, 1106-1131.

Zhang K, Hao L, Du M, Mi J, et al. 2017. A review on thermal stability and high temperature induced ageing mechanisms of solar absorber coatings. Renewable and Sustainable Energy Reviews 67, 1282-1299.

Zhu, X.W., Zhu L., Zhao, J.Q., 2017. Wavy-tape insert designed for managing highly concentrated solar energy on absorber tube of parabolic trough receiver. Energy 141, 1146-1155.

Zou, B., Dong, J.K., Yao, Y., Jiang, Y.Q., 2017. A detailed study on the optical performance of parabolic trough solar collectors with Monte Carlo Ray Tracing method based on theoretical analysis. Solar Energy 147, 189-201.

Figures:

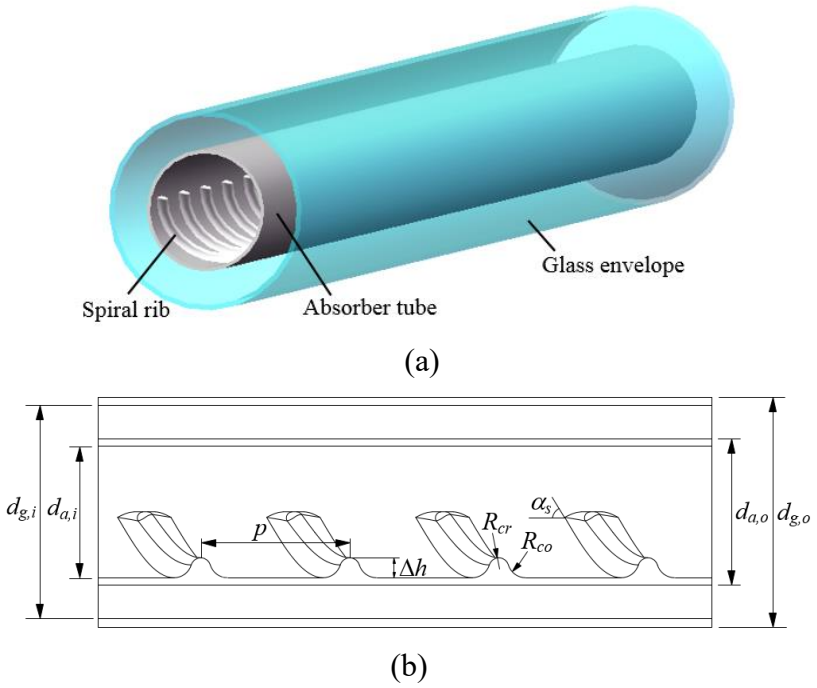

Fig. 1 Schematic of the USR-PTR: (a) three dimensional diagram (b) longitudinal section

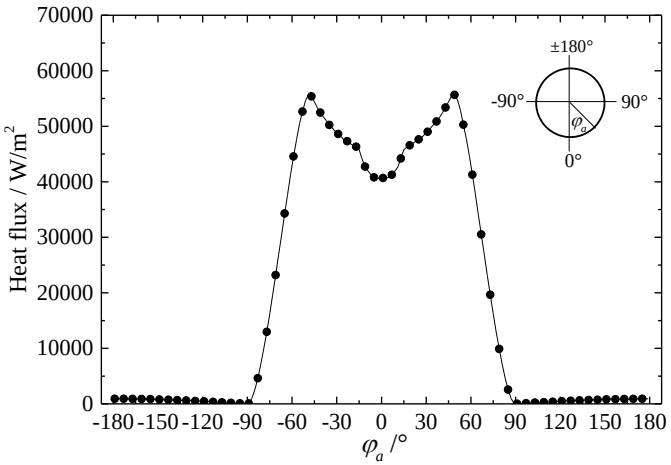

Fig. 2 Circumferential heat flux distribution on the absorber outer wall obtained by MCRT

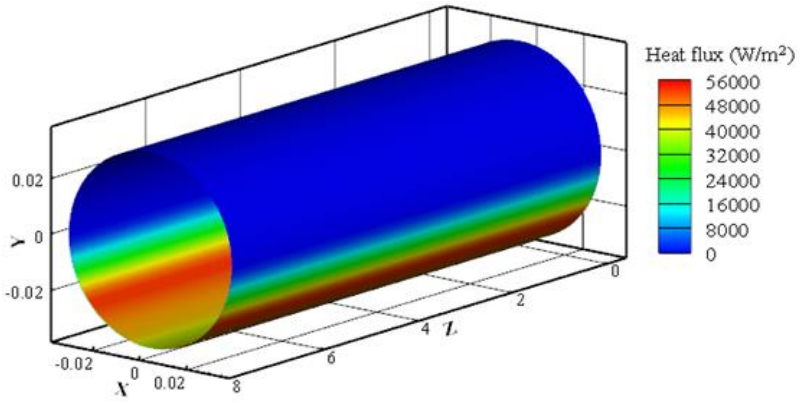

Fig. 3 Contour of the circumferential heat flux distribution on the absorber outer surface added by UDF

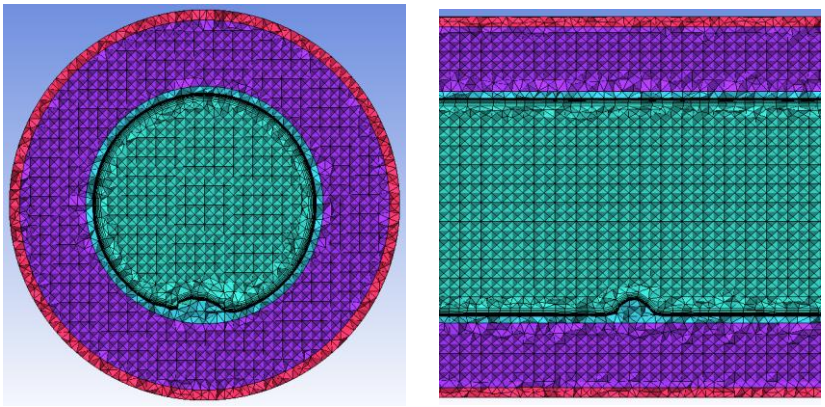

(a) (b)

Fig. 4 The schematic of domain discretization (meshing) of the receiver tube: (a) cross section, (b) longitudinal section

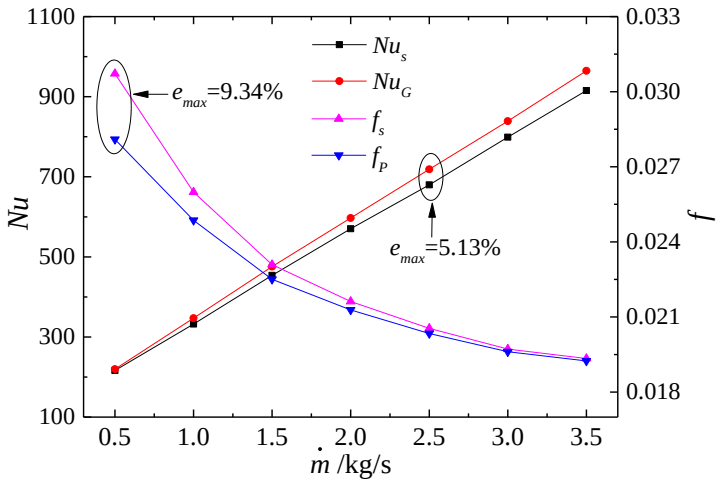

Fig. 5 Comparison of the results between simulation and empirical formulas

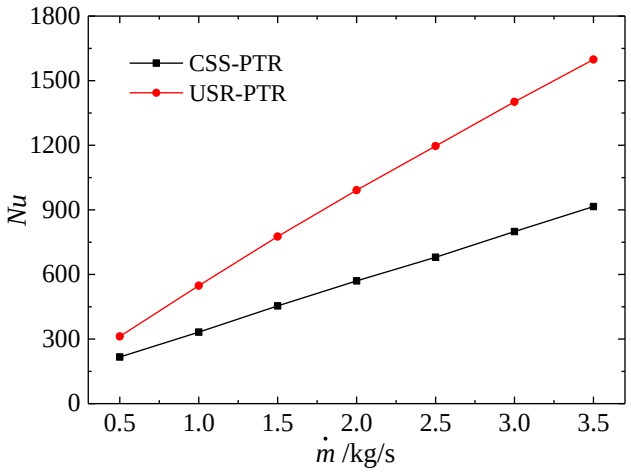

Fig. 6 Variation of the Nusselt number (*Nu*) with mass flow rate ($\dot{m}$)

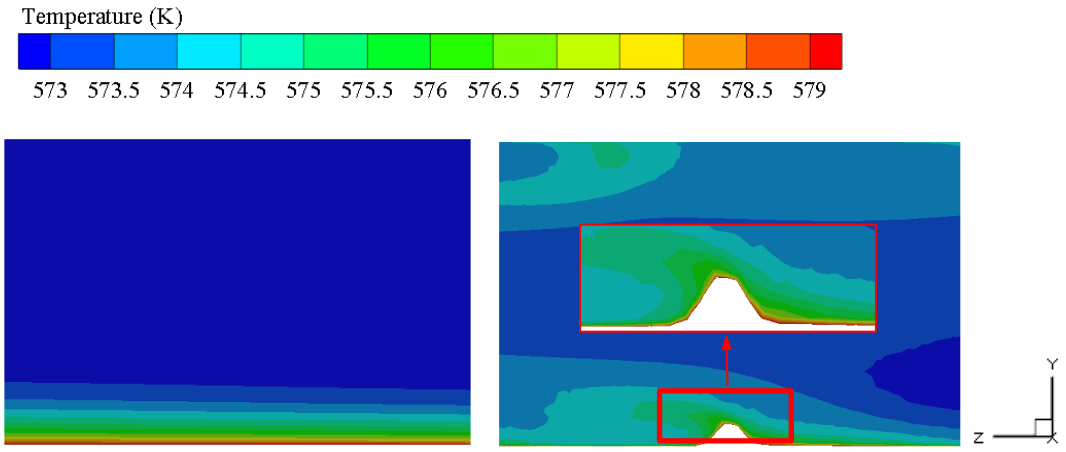

(a) (b)

Fig. 7 Distribution of the fluid temperature in the longitudinal section under condition of $\dot{m}$ =2 kg/s: (a) CSS-PTR, (b) USR-PTR

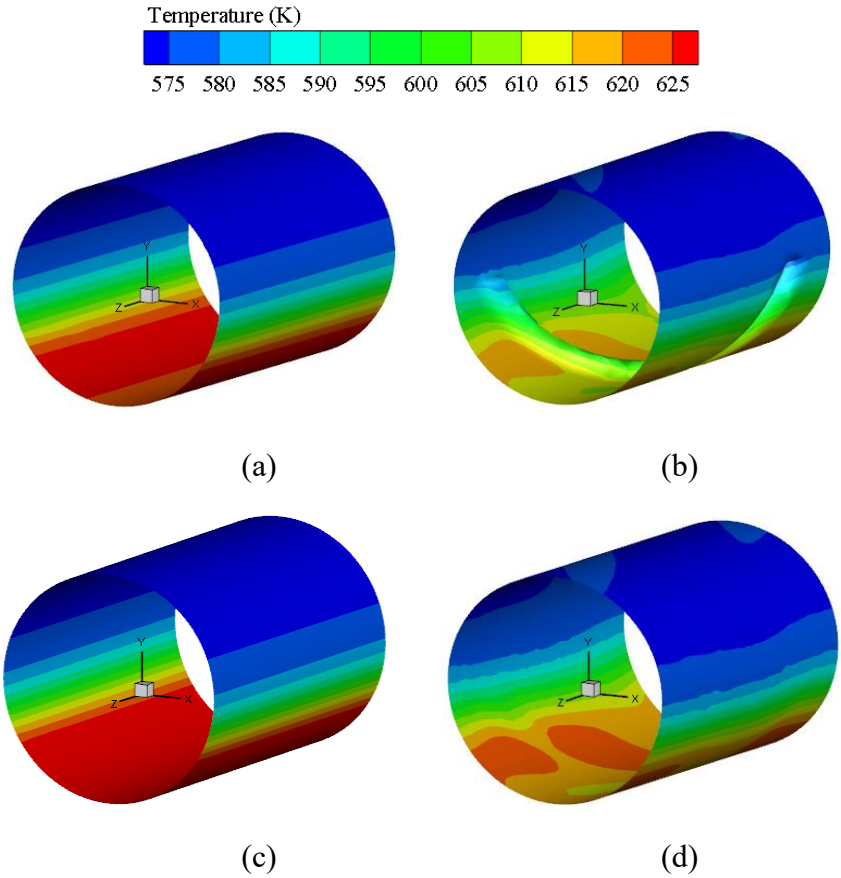

Fig. 8 Distribution of the absorber temperature under condition of $\dot{m}$ =2 kg/s: (a) inner surface of the CSS-PTR, (b) inner surface of the USR-PTR, (c) outer surface of the CSS-PTR, (d) outer surface of the USR-PTR

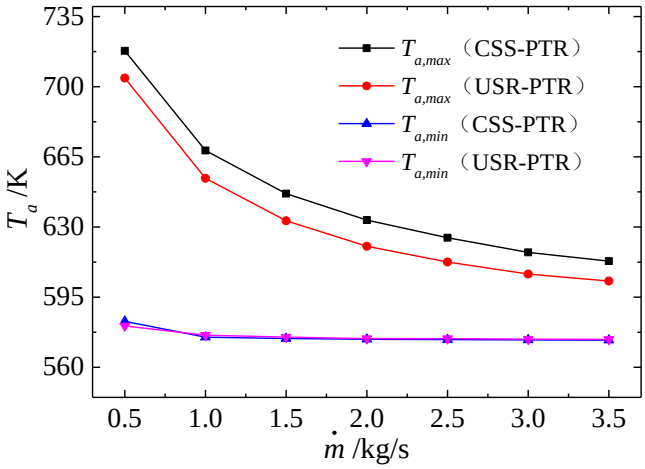

Fig. 9 Variation of the maximum ($T_{a,max}$) and minimum ($T_{a,min}$) temperature of the absorber at z=600 mm with mass flow rate ($\dot{m}$)

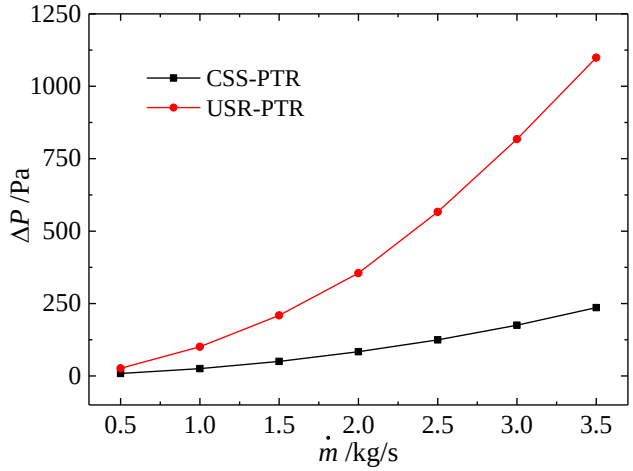

Fig. 10 Variation of the pressure drop (ΔP) with mass flow rate ($\dot{m}$)

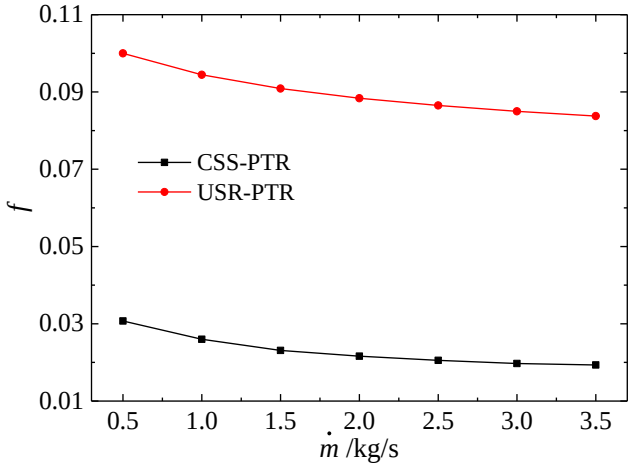

Fig. 11 Variation of the friction factor (f) with mass flow rate ($\dot{m}$)

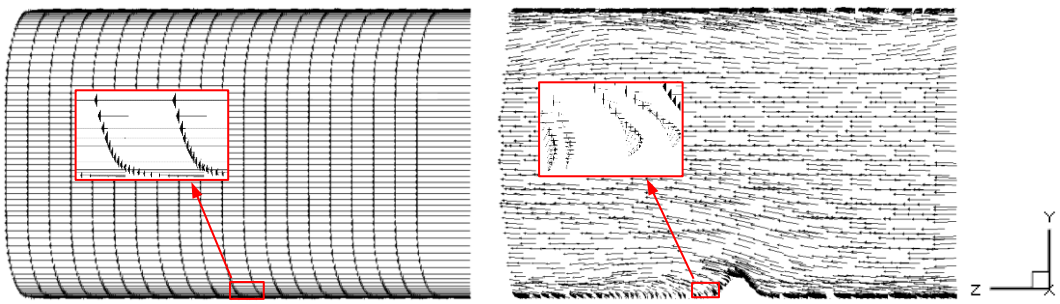

(a) (b)

Fig. 12 Diagram of the fluid velocity vector in the longitudinal section under condition of $\dot{m}$ =2 kg/s: (a) CSS-PTR, (b) USR-PTR

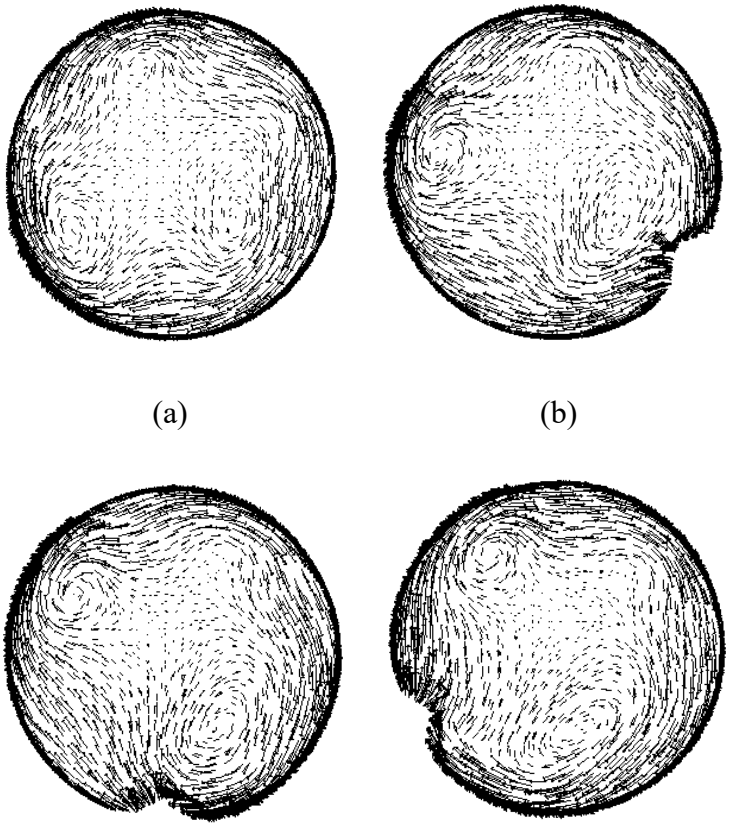

(a) (b)

(c) (d)

Fig. 13 Diagram of the fluid velocity vector in different cross sections of the USR-PTR under condition of $\dot{m}$ =2 kg/s: (a) z=600 mm, (b) z=630 mm, (c) z=650 mm, (d) z=670 mm

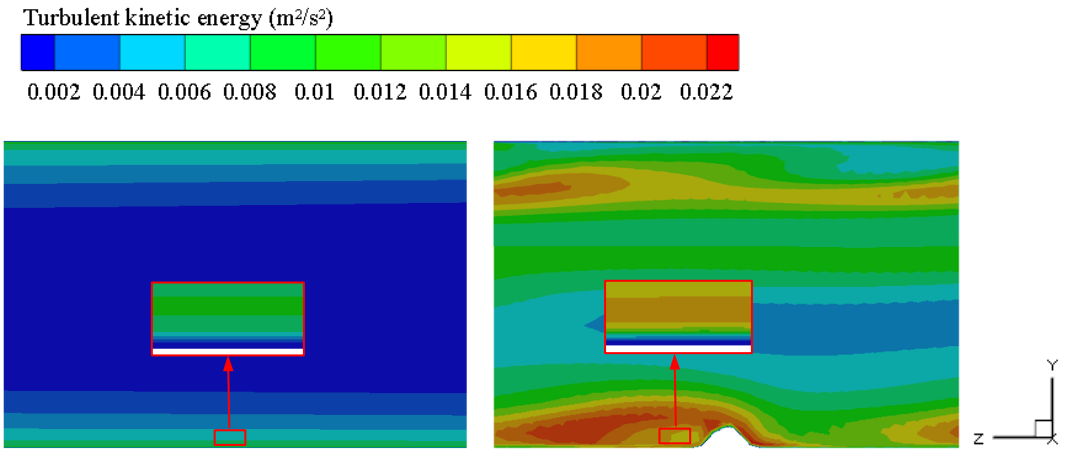

(a) (b)

Fig. 14 Distribution of the turbulent kinetic energy (TKE) in the longitudinal section under condition of $\dot{m}$ =2 kg/s: (a) CSS-PTR, (b) USR-PTR

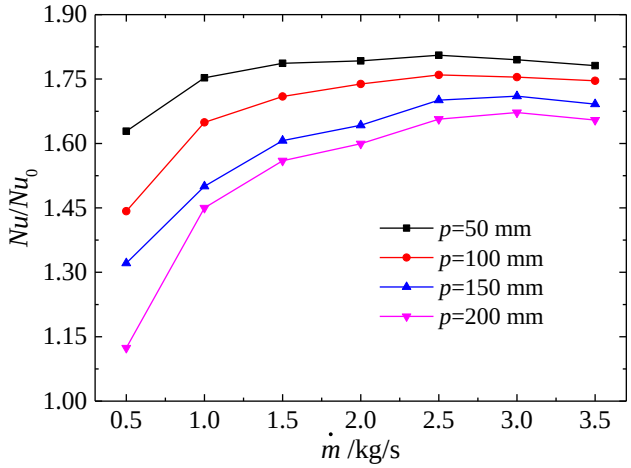

Fig. 15 Variation of Nu/Nu_0 with mass flow rate ($\dot{m}$) under different pitch intervals (p)

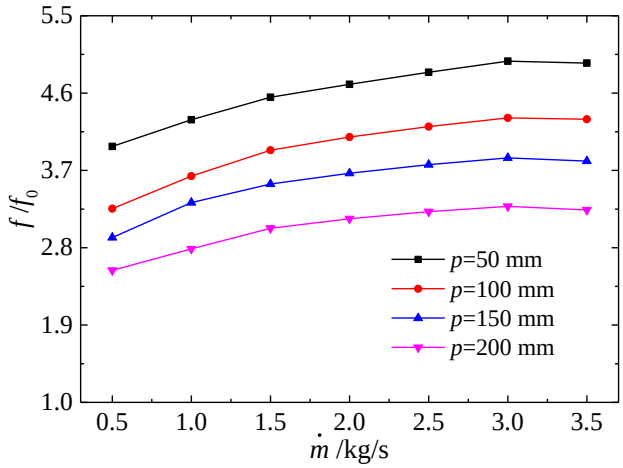

Fig. 16 Variation of f/f_0 with mass flow rate ($\dot{m}$) under different pitch intervals (p)

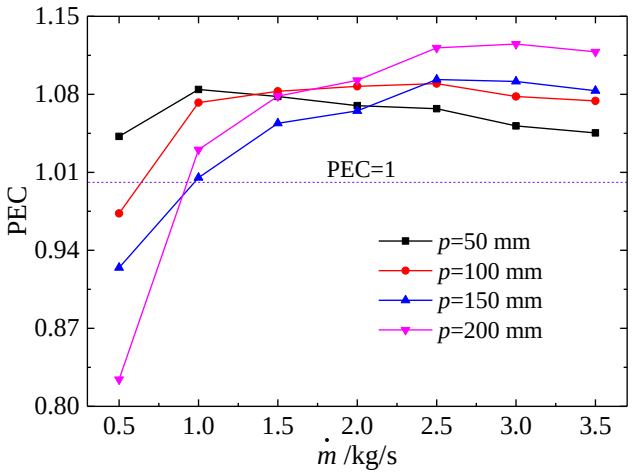

Fig. 17 Variation of PEC with mass flow rate ($\dot{m}$) under different pitch intervals (p)

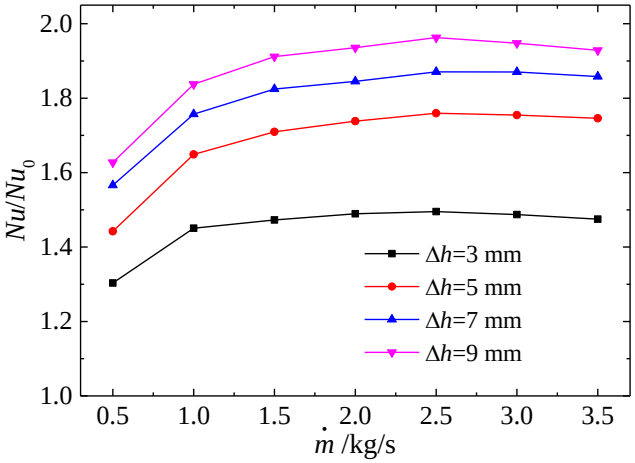

Fig. 18 Variation of Nu/Nu_0 with mass flow rate ($\dot{m}$) under different rib heights (Δh)

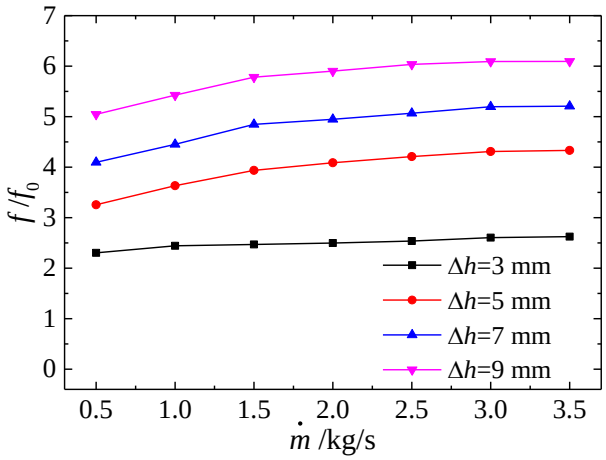

Fig. 19 Variation of f/f_0 with mass flow rate ($\dot{m}$) under different rib heights (Δh)

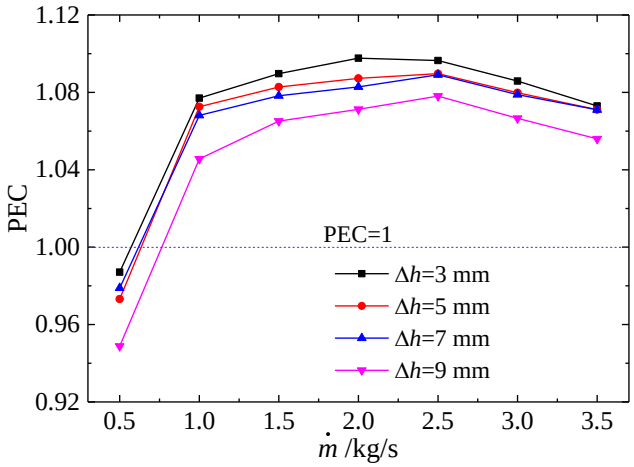

Fig. 20 Variation of PEC with mass flow rate ($\dot{m}$) under different rib heights (Δh)

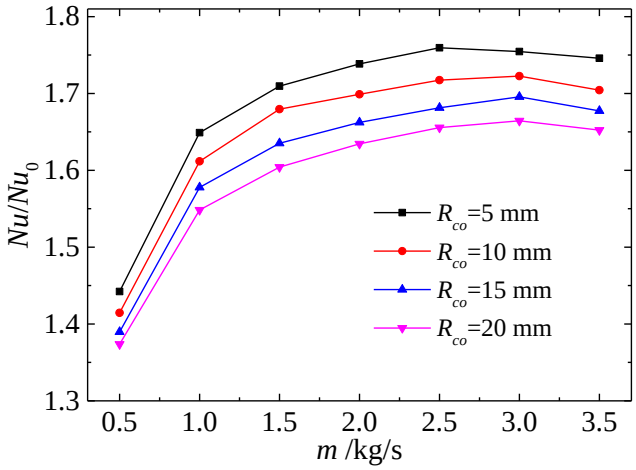

Fig. 21 Variation of Nu/Nu_0 with mass flow rate ($\dot{m}$) under different corner radiuses (R_{co})

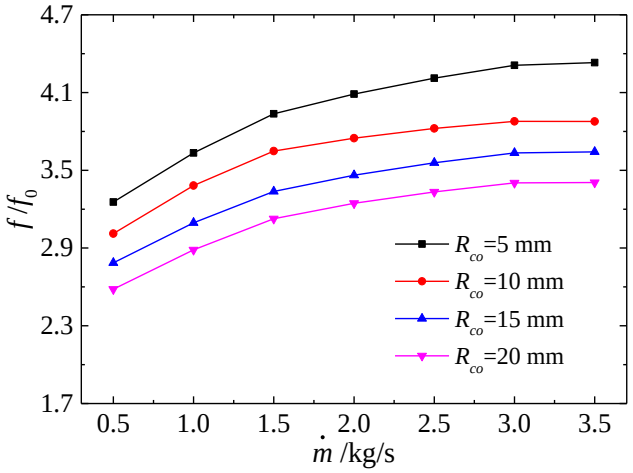

Fig. 22 Variation of f/f_0 with mass flow rate ($\dot{m}$) under different corner radiuses (R_{co})

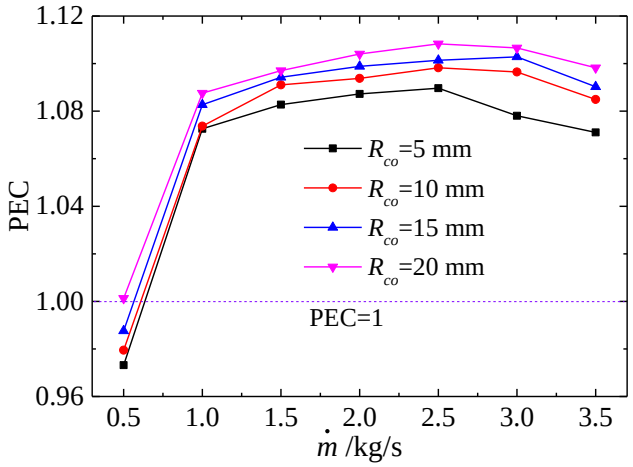

Fig. 23 Variation of PEC with mass flow rate ($\dot{m}$) under different corner radiuses (R_{co})

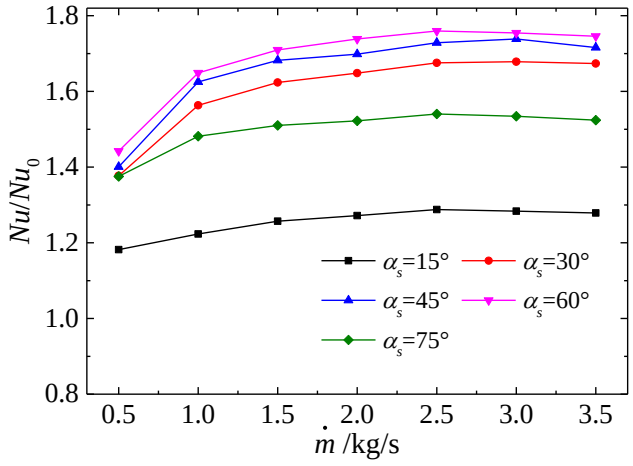

Fig. 24 Variation of Nu/Nu_0 with mass flow rate ($\dot{m}$) under different spiral angles (α_s)

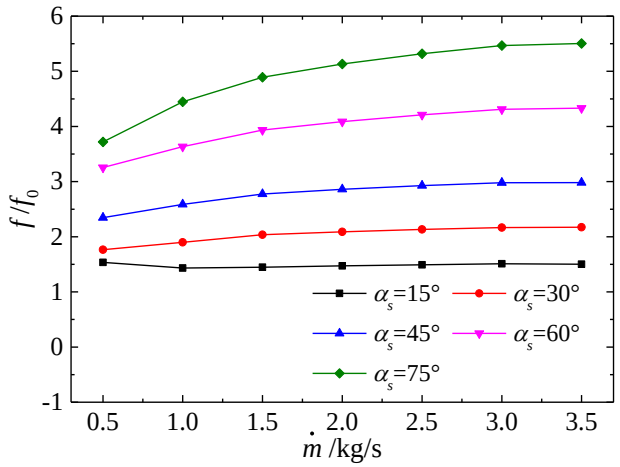

Fig. 25 Variation of f/f_0 with mass flow rate ($\dot{m}$) under different spiral angles (α_s)

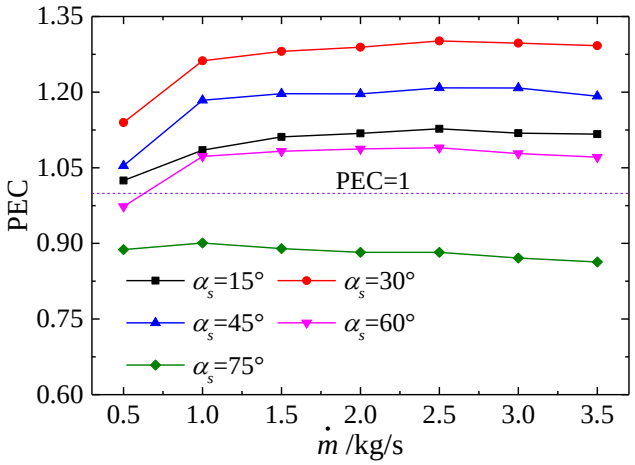

Fig. 26 Variation of PEC with mass flow rate ($\dot{m}$) under different spiral angles (α_s)

Tables:

Table 1 Parameters of SEGS LS-2 PTC module (Dudley et al., 1994)

Parameter	Value	Unit
W_c	5	m
f_c	1.84	m
L_c	7.8	m
$d_{a,i}$	0.066	m
$d_{a,o}$	0.07	m
$d_{g,i}$	0.109	m
$d_{g,o}$	0.115	m
α_a	0.96	——
ρ_r	0.93	——
τ_g	0.95	——

Table 2 Constants in the turbulence model (Tao, 2001)

C_1	C_2	C_μ	σ_k	σ_ε
1.42	1.68	0.0845	0.719	0.719

Table 3 Thermophysical parameters of Syltherm 800 (Agustin et al., 2007)

Parameters	Fitting formula
Density (kg/m^3)	$\rho = -6.061657\times10^{-4}T^2 - 0.4153495T + 1105.702$
Specific heat (J/kg·K)	$c_p = 1.708T + 1.107798$
Thermal conductivity (W/m·K)	$\lambda = -5.753496\times10^{-10}T^2 - 1.875266\times10^{-4}T + 0.190021$
Dynamic viscosity (Pa·s)	$\mu = 6.672331\times10^{-13}T^4 - 1.56003\times10^{-9}T^3 + 1.388285\times10^{-6}T^2 - 5.541277\times10^{-4}T + 0.08486612$

Table 4 The structural parameters of the USR-PTR used for grid independence checking

p (mm)	Δh (mm)	R_{cr} (mm)	R_{co} (K)	α_s (°)
100	5	3	5	60

Table 5 Results for grid independence checking

Grid system	T_{out} (K)	Nu_{ave}	f_{ave}
420000	576.44	997.97	0.07991
710000	575.56	995.84	0.08454
900000	574.75	992.28	0.08719
1130000	574.33	991.38	0.08838
1210000	574.37	991.45	0.08841
1570000	574.32	991.21	0.08837

Table 6 Typical cases selected from Ref. (Dudley, et al., 1994) for model validation

Case	I_D (W/m^2)	m (kg/s)	v_{amb} (m/s)	T_{amb} (K)	T_{in} (K)	$T_{out,t}$ (K)
1	933.7	0.6782	2.6	294.35	375.35	397.15
2	937.9	0.6206	1.0	301.95	570.95	590.05
3	968.2	0.6536	3.7	295.22	424.15	446.45
4	813.1	0.7254	3.6	298.95	374.35	392.15
5	858.4	0.7207	3.1	300.75	427.45	444.85
6	896.4	0.664	0.9	303.15	523.85	540.95

Table 7 Comparison of results between simulation and test

Case	T_{in} (K)	$T_{out,t}$ (K)	$T_{out,s}$ (K)	$\lvert T_{out,t} - T_{in} \rvert$ (K)	$\lvert T_{out,s} - T_{out,t} \rvert$ (K)	e_T (%)
1	375.35	397.15	399.38	21.8	2.23	10.23
2	570.95	590.05	591.84	19.1	1.79	9.37
3	424.15	446.45	448.25	22.3	1.8	8.07
4	374.35	392.15	393.79	17.8	1.64	9.21
5	427.45	444.85	446.03	17.4	1.18	6.78
6	523.85	540.95	542.46	17.1	1.51	8.83

Table 8 Mass flow rate and the corresponding inlet Reynolds number

m (kg/s)	0.5	1	1.5	2	2.5	3	3.5
Re	20254	40508	60763	81017	101272	121526	141781